PCCP

PAPER

View Article Online
View Journal | View Issue

Cite this: *Phys. Chem. Chem. Phys.*, 2024, **26**, 25385

Excited-state aromaticity reversals in norcorrole†

Peter B. Karadakov * and Edward Cummings

Received 13th August 2024,
Accepted 19th September 2024

DOI: 10.1039/d4cp03198a

rsc.li/pccp

Aromaticity reversals between the electronic ground state (S_0) and the lowest triplet (T_1) and singlet (S_1) excited states of Ni^{II} norcorrole (NiNc) and norcorrole (H_2Nc) are investigated by comparing the HOMA (harmonic oscillator model of aromaticity) values at the optimized S_0, T_1 and S_1 geometries, and by analysing the changes in the nucleus-independent chemical shift (NICS) values and in the isotropic magnetic shielding distributions between the S_0 and T_1 states. The results strongly suggest that the antiaromatic features of the S_0 states of the NiNc and H_2Nc molecules, two very similar antiaromatic "internal crosses", undergo aromaticity reversals upon excitation to T_1 or S_1 and merge with the aromatic peripheries to produce Baird-aromatic systems with 24 π electrons each. Somewhat counterintuitively, the geometries of the fully aromatic T_1 and S_1 states of NiNc and H_2Nc turn out to have larger bowl depths and so are more non-planar than the corresponding S_0 geometries at which both molecules display antiaromatic features.

Introduction

Norcorrole (H_2Nc), the smallest cyclic tetrapyrrole porphyrin analogue synthesized to date,[1,2] was first conceived theoretically using DFT calculations.[3] According to the results of a magnetic shielding study,[4] H_2Nc and its more popular Ni^{II} complex (NiNc) feature, in their electronic ground states (S_0), very similar strongly deshielded antiaromatic "internal crosses". The boundary of the antiaromatic "internal cross" in NiNc follows the conjugation pathway in Fig. 1(a). The stability of NiNc and H_2Nc is explained through the presence of an aromatic "halo" in the form of increased shielding over a peripheral conjugation pathway, which can be thought to involve either 18 atoms and 18 π electrons (Fig. 1(c)), or 14 atoms and 14 π electrons, bypassing the C_α–C_α bonds through homoconjugation (Fig. 1(d)).[4] The alternative antiaromatic conjugated pathway in Fig. 1(b) which is often depicted in the literature[2,3,5,6] provides no explanation for the stability of this type of molecule.

Since the formulation of Baird's rule,[7] which states that the familiar Hückel $4n + 2$ and $4n$ rules for S_0 aromaticity in cyclic conjugated hydrocarbons are reversed in the lowest triplet ππ* state (usually T_1) so that aromatic rings become those with $4n$ π electrons and the antiaromatic rings include $4n + 2\pi$ electrons,

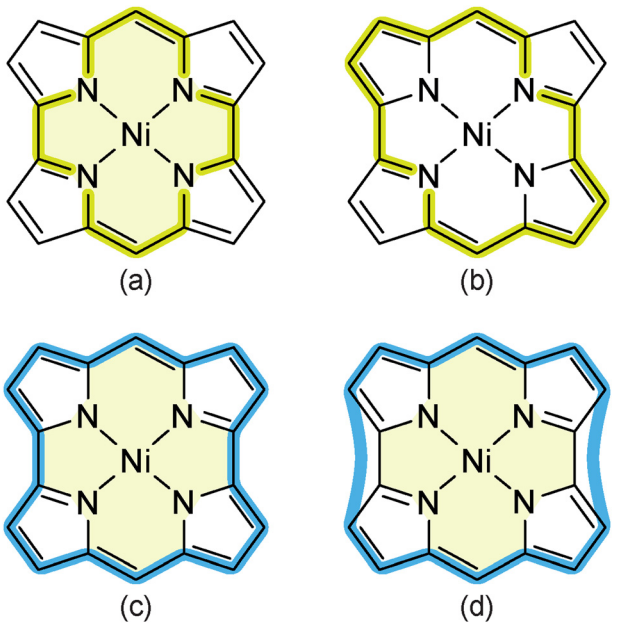

Fig. 1 Conjugation pathways in NiNc. (a) Antiaromatic "internal cross" (ic), with 14 atoms and 16 π electrons; (b) antiaromatic, with 16 atoms and 16 π electrons; (c) and (d) aromatic peripheral (p), with 18 atoms and 18 π electrons, or with 14 atoms and 14 π electrons. The deshielded area within the "internal cross" is shaded in (a), (c) and (d). Adapted with permission from P. B. Karadakov, *Org. Lett.*, 2020, **22**, 8676–8680. Copyright 2020 American Chemical Society.

Department of Chemistry, University of York, Heslington, York, YO10 5DD, UK. E-mail: peter.karadakov@york.ac.uk

† Electronic supplementary information (ESI) available: Gaussian cube files with isotropic shielding values for the T_1 states of NiNc and H_2Nc; additional computational details; TDA-PBE0 and TDA-ωB97X vertical excitation energies; natural population analysis charges; Cartesian coordinates for the S_1 and T_1 optimized geometries of NiNc and H_2Nc and the corresponding energies, lowest harmonic frequencies and $\langle S^2 \rangle$ values for UB3LYP calculations. See DOI: https://doi.org/10.1039/d4cp03198a

excited state aromaticity reversals have become an area of intensive experimental and theoretical research. These phenomena have been found to have a wide range of applications including designing molecules with light-controllable behaviour, molecular photoswitches,[8] molecular motors,[9,10] ''flapping'' fluorophores,[11–13] and rationalizing experimental evidence about photochemical reactions, for example, excited-state intramolecular proton transfers;[14,15] further information on excited state aromaticity reversals is provided in several reviews.[16–18] Aromaticity reversals similar to those predicted by Baird's rule have been shown to occur between S_0 and the lowest singlet $\pi\pi^*$ excited state (usually S_1).[19–21]

Having in mind Baird's rule and the electron counts for the conjugation pathways in Fig. 1, it is intriguing to find out if and how the competing aromatic and antiaromatic features of the S_0 state of norcorrole change in its S_1 and T_1 states. If the S_1 and T_1 states turn out to be aromatic, will this be sufficient to make the respective geometries of NiNc and H_2Nc planar? The theoretical estimate of the vertical $S_1 \leftarrow S_0$ vertical excitation energy of NiNc of just about 0.8 eV[22] suggests that the S_1 state might be benefitting from aromatic stabilization.

In this paper we investigate the aromaticity reversals between the S_0 and T_1, and S_0 and S_1 states of NiNc and H_2Nc by comparing the optimized geometries of these states with the help of HOMA (harmonic oscillator model of aromaticity),[23–25] and by analysing the changes in the values of the respective nucleus-independent chemical shifts (NICS)[26–28] for the pyrrole rings and the 6-membered rings within the ''internal cross'' between the S_0 and T_1 states, as well as the changes in the respective spatial variations in off-nucleus isotropic magnetic shielding, $\sigma_{iso}(\mathbf{r}) = \frac{1}{3}[\sigma_{xx}(\mathbf{r}) + \sigma_{yy}(\mathbf{r}) + \sigma_{zz}(\mathbf{r})]$, within molecular space.

Computational details

All geometry optimizations, analytical harmonic frequency, shielding and natural population analysis (NPA) calculations reported in this paper were carried out in the gas phase using Gaussian.[29] The optimized geometries were confirmed as local minima through analytical harmonic frequency calculations. The S_0 geometries of NiNc and H_2Nc optimized at the B3LYP-D3(BJ)/def2-TZVP level (spin-restricted RB3LYP with Grimme's D3 dispersion corrections and Becke–Johnson damping) were taken from ref. 4. $T_1 \leftarrow S_0$ and $S_1 \leftarrow S_0$ vertical excitation energies (VEEs) were calculated with the TDA-B3LYP, TDA-PBE0 and TDA-ωB97X methods (Tamm–Dancoff approximation combined with B3LYP, PBE0 and ωB97X, respectively), in the def2-TZVP basis set, at the S_0 B3LYP-D3(BJ)/def2-TZVP geometries. The $T_1 \leftarrow S_0$ vertical excitation energies were also calculated using triplet spin-unrestricted B3LYP, UB3LYP/def2-TZVP. The geometries of the T_1 and S_1 states of NiNc and H_2Nc were optimized at the TDA-B3LYP-D3(BJ)/def2-TZVP level. The geometries of the T_1 states were also optimized at the triplet UB3LYP-D3(BJ)/def2-TZVP level. The decision to use TDA-B3LYP rather than time-dependent B3LYP (TD-B3LYP) follows from recommendations in the literature.[30,31]

HOMA calculations were performed with Multiwfn[32] using the default parametrization. The decision to use the default parametrization rather than HOMER, a reparameterization of HOMA for triplet excited states,[33] is associated with the need to compare the aromaticity levels at the optimized S_0, T_1 and S_1 geometries of NiNc and H_2Nc.

S_0 NICS values and Gaussian cube files with isotropic shielding volume data calculated at the B3LYP-GIAO/6-311++G(d,p) level (B3LYP with gauge-including atomic orbitals) were taken from ref. 4. T_1 NICS values corresponding to vertical excitations were calculated using triplet UB3LYP-GIAO/6-311++G(d,p) at the S_0 B3LYP-D3(BJ)/def2-TZVP geometries. T_1 NICS values and volume data needed for the T_1 isotropic shielding isosurfaces at the T_1 triplet UB3LYP-D3(BJ)/def2-TZVP optimized geometries were obtained using triplet UB3LYP-GIAO/6-311++G(d,p) calculations. The S_0 $\sigma_{iso}(\mathbf{r})$ volume data from ref. 4 as well as the T_1 $\sigma_{iso}(\mathbf{r})$ volume data computed in this paper make use of regular three-dimensional grids of data points with a spacing of 0.1 Å. Similarly to the procedure followed in ref. 4, to reduce computational effort, the T_1 shielding tensors for H_2Nc and NiNc were calculated at symmetry-unique data points only, then data for each molecule were replicated through symmetry operations to complete the grid and assembled in a Gaussian cube file.

The optimized geometries of the T_1 states of NiNc and H_2Nc are non-planar and the standard recipes for calculating NICS(0)[26] as $-\sigma_{iso}$(at the ring centre) and NICS(1)[27,28] as $-\sigma_{iso}$ (at 1 Å above the ring centre) need adjustment. The NICS(0) positions at these geometries were chosen as the averages of the coordinates of the ring atoms; in order to calculate a pair of NICS(±1) values, a plane was fitted to the coordinates of the ring atoms and the NICS(0) position, and the NICS(±1) positions were taken as the points 1 Å above and below that plane along the normal passing through the NICS(0) position following the procedure outlined in ref. 34 and 35.

As usual in NICS and ring current calculations on triplet systems (see, for example, ref. 36 and 37), the UB3LYP-GIAO magnetic properties of the triplet states of thiophene computed in this paper include the contributions arising from the perturbation to the Kohn–Sham orbitals only. The omission of the large terms arising from the interaction of the electronic spin angular momentum with the magnetic field[38,39] implies that the reported numbers will exhibit considerable differences from experimental measurements if and when such measurements become available. The advantage of the approach adopted here is that the values reported for triplet states can be compared directly to those for singlet states.

The T_1 Gaussian cube files with shielding data, additional computational details, TDA-PBE0 and TDA-ωB97X VEEs, NPA charges, and all S_1 and T_1 optimized geometries and the corresponding energies, lowest harmonic frequencies and $\langle S^2 \rangle$ values for UB3LYP calculations are included in the (ESI†). The $\sigma_{iso}(\mathbf{r})$ volume data provided in the Gaussian cube files allow inspection of various aspects of the shielding distributions around the T_1 states of NiNc and H_2Nc, including construction of shielding isosurfaces at different $\sigma_{iso}(\mathbf{r})$ values, $\sigma_{iso}(\mathbf{r})$ contour plots in various planes and $\sigma_{iso}(\mathbf{r})$ scans along various directions.

Results and discussion

An investigation of the gas-phase ground state potential energy surfaces of NiNc and H_2Nc at the B3LYP-D3(BJ)/def2-TZVP level[1] showed that the potential energy surface of NiNc has two equivalent bowl-shaped geometries of C_{2v} symmetry, connected through a planar transition state (TS) of D_{2h} symmetry; the potential energy surface of H_2Nc features two pairs of local minima, comprised of two equivalent geometries of C_i symmetry and of two bowl-shaped geometries of C_{2v} symmetry, respectively, and a planar 2nd-order saddle point (SOS) which acts as a TS for both the bowl-to-bowl inversion between the two C_2 local minima, and for the flip between the two C_i local minima.

The current results for the gas-phase T_1 and S_1 potential energy surfaces of NiNc show that, similarly to the S_0 potential energy surface, each of these potential energy surfaces has two equivalent bowl-shaped local minima of C_{2v} symmetry, connected through a planar TS of D_{2h} symmetry. The very small NiNc S_0 inversion barrier of 0.7 kcal mol^{-1} increases to 1.4 kcal mol^{-1} in T_1, at both the UB3LYP-D3(BJ) and TDA-B3LYP-D3(BJ) levels, and to 1.7 kcal mol^{-1} in S_1, at the TDA-B3LYP-D3(BJ) level. The gas-phase T_1 and S_1 potential energy surfaces of H_2Nc were found to have two equivalent bowl-shaped local minima of C_2 symmetry, connected through a TS of C_i symmetry. The H_2Nc bowl-to-bowl S_0 inversion barrier of 2.0 kcal mol^{-1} increases to 3.2 and 3.1 kcal mol^{-1} in T_1, at the UB3LYP-D3(BJ) and TDA-B3LYP-D3(BJ) levels, respectively, and to 4.6 kcal mol^{-1} in S_1, at the TDA-B3LYP-D3(BJ) level.

The more important bond lengths from the S_0 B3LYP-D3(BJ), T_1 UB3LYP-D3(BJ) and TDA-B3LYP-D3(BJ), and S_1 TDA-B3LYP-D3(BJ) local minimum geometries of NiNc (C_{2v}) and H_2NiNc (C_2) are shown in Fig. 2.

The most noticeable change in the geometries of NiNc and H_2Nc upon excitation from S_0 to T_1 or S_1 is the shortening of the C_α–C_α bonds. All other C–C and bonds C–N bonds are also affected by excitation, to different extents. On the other hand, the Ni–C distances and the C–H bond lengths within the "internal cross" of H_2Nc remain much the same in all three states. In parallel with the shortening of the C_α–C_α bonds upon excitation, we observe increases in the inversion barriers and in the bowl depths of NiNc and H_2Nc, measured as the difference between the largest and the smallest atomic z coordinates (the z axes coincide with the C_2 symmetry axes at the C_{2v} NiNc and C_2 H_2Nc local minimum geometries). These increases in bowl depth (Table 1) can be viewed as attempts of the respective structures to alleviate the additional strain caused by the shortening of the C_α–C_α bonds. The larger bowl depths at the S_0, T_1 and S_1 local minimum geometries of H_2Nc can be explained by the steric repulsion between the hydrogens within the "internal cross".

Table 1 Bowl depths at the S_0 B3LYP-D3(BJ), T_1 U ≡ UB3LYP-D3(BJ), T_1 TDA ≡ TDA-B3LYP-D3(BJ) and S_1 TDA ≡ TDA-B3LYP-D3(BJ) local minimum geometries of NiNc and H_2Nc (in Å)

Molecule	S_0	T_1 U	T_1 TDA	S_1 TDA
NiNc	0.912	1.082	1.082	1.149
H_2Nc	1.496	1.576	1.580	1.710

The features of the S_0, T_1 and S_1 optimized geometries of NiNc and H_2Nc can be compared conveniently using the HOMA values for the conjugation pathways following the "internal cross", Fig. 1(a), and the periphery, Fig. 1(c), reported in Table 2. We note that all HOMA values from Table 1 suggest different levels of aromaticity and HOMA does not detect the ground-state antiaromatic characters of the "inner crosses". The sizeable increases in the HOMA values for the two "internal crosses" on passing from S_0 to T_1 or S_1 are indications of marked decreases in bond length alternation which are most commonly associated with marked increases in aromaticity.

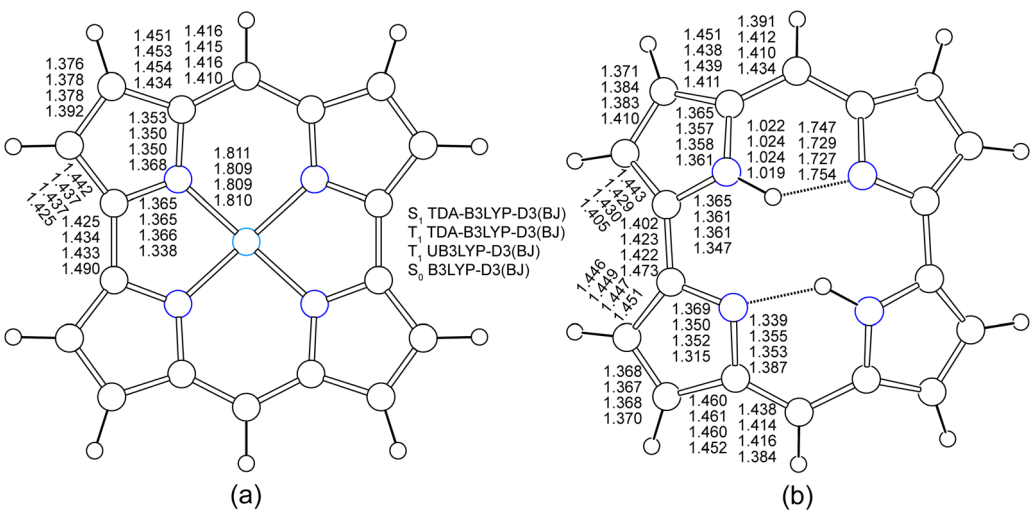

Fig. 2 Selected symmetry unique bond lengths (in Å) from the S_0, T_1 and S_1 local minimum geometries of (a) NiNc and (b) H_2Nc, arranged in columns of four numbers each including, from bottom to top, S_0 B3LYP-D3(BJ), T_1 UB3LYP-D3(BJ), T_1 TDA-B3LYP-D3(BJ) and S_1 TDA-B3LYP-D3(BJ) results. (a) and (b) show the S_0 B3LYP-D3(BJ) NiNc (C_{2v}) and H_2Nc (C_2) local minimum geometries, looking at the top of each bowl.

Table 2 HOMA values for the "internal cross" (ic) and peripheral (p) conjugation pathways at the S_0 B3LYP-D3(BJ), T_1 U ≡ UB3LYP-D3(BJ), T_1 TDA ≡ TDA-B3LYP-D3(BJ) and S_1 TDA ≡ TDA-B3LYP-D3(BJ) optimized geometries of NiNc and H_2Nc

Pathway	Geometry	S_0	T_1 U	T_1 TDA	S_1 TDA
NiNc (ic)	C_{2v}	0.550	0.834	0.833	0.858
	D_{2h} (TS)	0.467	0.774	0.773	0.799
NiNc (p)	C_{2v}	0.475	0.504	0.505	0.513
	D_{2h} (TS)	0.382	0.409	0.408	0.408
H_2Nc (ic)	C_2	0.602	0.883	0.883	0.860
	C_i (T_1/S_1 TS)	0.580	0.840	0.838	0.821
	C_{2h} (S_0 SOS)	0.524			
H_2Nc (p)	C_2	0.455	0.544	0.539	0.459
	C_i (T_1/S_1 TS)	0.451	0.473	0.470	0.419
	C_{2h} (S_0 SOS)	0.372			

The HOMA values for the peripheries of NiNc and H_2Nc also increase, but much more modestly, on passing from S_0 to T_1 or S_1. The HOMA values for the planar D_{2h} TS geometries of NiNc, the planar C_{2h} SOS in S_0 H_2Nc, and the C_i TS geometries of H_2Nc in its S_1 and T_1 states are smaller than those at the local minima connected by these TS and SOS geometries. This is an indication that the energy decreases on passing from these TS and SOS geometries to the respective local minima can be associated with additional aromatic stabilization despite the parallel loss of planarity in the S_0, T_1 and S_1 states of NiNc, and in the S_0 state of H_2Nc. The very close HOMA values obtained for the T_1 states of NiNc and H_2Nc at the UB3LYP-D3(BJ) and TDA-B3LYP-D3(BJ) optimized geometries highlight the similarity between these geometries; the HOMA values for the T_1 and S_1 states of the two molecules at the respective TDA-B3LYP-D3(BJ) optimized geometries also suggest reasonable levels of similarity between the geometries of these states. The HOMA values depend on bond lengths only and do not account for the increase in bowl depth upon excitation of NiNc and H_2Nc from S_0 to T_1 or S_1. While the decrease in the extent of bond alternation upon excitation favours aromaticity, the increase in bowl depth which makes the structures less planar, does not do so as it hinders conjugation. We note that HOMA cannot be used to examine the aromaticity changes associated with vertical excitations which utilize the S_0 geometries.

The symmetries of the TDA-B3LYP descriptions of the T_1//S_0, S_1//S_0, T_1//T_1 and S_1//S_1 states of NiNc and H_2Nc (the S_0 B3LYP or T_1 or S_1 TDA-B3LYP local minimum geometry, of C_{2v} and C_2 symmetry for NiNc and H_2Nc, respectively, is shown after the double slash) are identical, A_2 for NiNc and A for H_2Nc. The symmetries of the triplet UB3LYP Kohn–Sham determinants for the T_1//S_0 and T_1//T_1 states of the two molecules (with T_1//T_1 utilizing the respective triplet UB3LYP local minimum geometries) coincide with those of the corresponding TDA-B3LYP descriptions. All of the TDA-B3LYP excited state descriptions are dominated by the HOMO → LUMO orbital excitations.

The very low T_1 ← S_0 and S_1 ← S_0 TDA-B3LYP and UB3LYP vertical (VEE) and adiabatic (AEE) excitation energies of NiNc and H_2Nc (Table 3) suggest that the S_0 states of the two molecules experience antiaromatic destabilization, whereas the corresponding T_1 and S_1 states experience aromatic stabilization. For reference, the B3LYP HOMO–LUMO gaps at the C_{2v} NiNc and C_2 H_2Nc S_0 local minimum geometries are 1.480 and 1.654 eV, respectively. The T_1 ← S_0 and S_1 ← S_0 VEEs and AEEs obtained using other TDA-DFT and UDFT methods may show some differences, but the qualitative features of the TDA-B3LYP and UB3LYP descriptions of the T_1 and S_1 states of NiNc and H_2Nc are unlikely to change. For example, the VEEs calculated using TDA-PBE0 are in close agreement with their TDA-B3LYP counterparts, and the respective VEEs calculated using TDA-ωB97X are higher by between 0.156–0.449 eV but still fairly low (Table S1, ESI†); the TDA-PBE0 and TDA-ωB97X excited state descriptions continue to be dominated by the HOMO → LUMO orbital excitations.

Table 3 Vertical and adiabatic T_1 ← S_0 and S_1 ← S_0 excitation energies of NiNc and H_2Nc (in eV, U ≡ UB3LYP, TDA ≡ TDA-B3LYP)

State	VEE U	VEE TDA	AEE U	AEE TDA
NiNc T_1 ($1\ ^3A_2$)	0.501	0.458	0.295	0.259
NiNc S_1 ($1\ ^1A_2$)		0.841		0.608
H_2Nc T_1 ($1\ ^3A$)	0.671	0.607	0.380	0.338
H_2Nc S_1 ($2\ ^1A$)		0.999		0.635

The NICS values and carbon, nitrogen and proton isotropic shieldings for the S_0 and T_1 electronic states of NiNc and H_2Nc, computed using B3LYP-GIAO and UB3LYP-GIAO, respectively, are shown in Fig. 3. Obtaining such data for the S_1 states of the two molecules is a much more challenging task. CASSCF(2,2)-GIAO ("2 electrons in 2 orbitals" complete active space self-consistent field with GIAOs) calculations with several basis sets on the S_1 state of NiNc, utilizing the Hartree–Fock HOMO and LUMO as the initial guesses for the active space orbitals and carried out using Dalton,[40] were found to yield unphysical values for some of the nuclear isotropic shieldings (such as very low or even negative values for all proton isotropic shieldings). This is in contrast to the results of CASSCF(2,2)-GIAO calculations on the S_1 states of other molecules.[41] We expect that obtaining reasonable estimates of the quantities included in Fig. 3 for the S_1 states of the two molecules might require full π space CASSCF(24,24)-GIAO calculations; based on our experience with CASSCF-GIAO calculations (see, for example, ref. 42) we believe that such calculations are beyond the capabilities of the existing codes.

The NICS(0) and NICS(±1) values at positions in, above and below the "internal crosses" in NiNc and H_2Nc clearly show that the "internal crosses" in both molecules switch from antiaromatic to aromatic upon vertical excitation from S_0 to T_1 (compare the S_0//S_0 and T_1//S_0 results). In parallel, the NICS(0) and NICS(±1) values for the pyrrole rings indicate that these rings switch from moderately antiaromatic to moderately aromatic or aromatic (the pyrrole rings with hydrogen atoms in H_2Nc). Interestingly, geometry relaxation leads to relatively minor changes in the NICS values (compare the T_1//S_0 and T_1//T_1 results); while the general trend is towards more negative NICS values and higher levels of aromaticity, a small number of

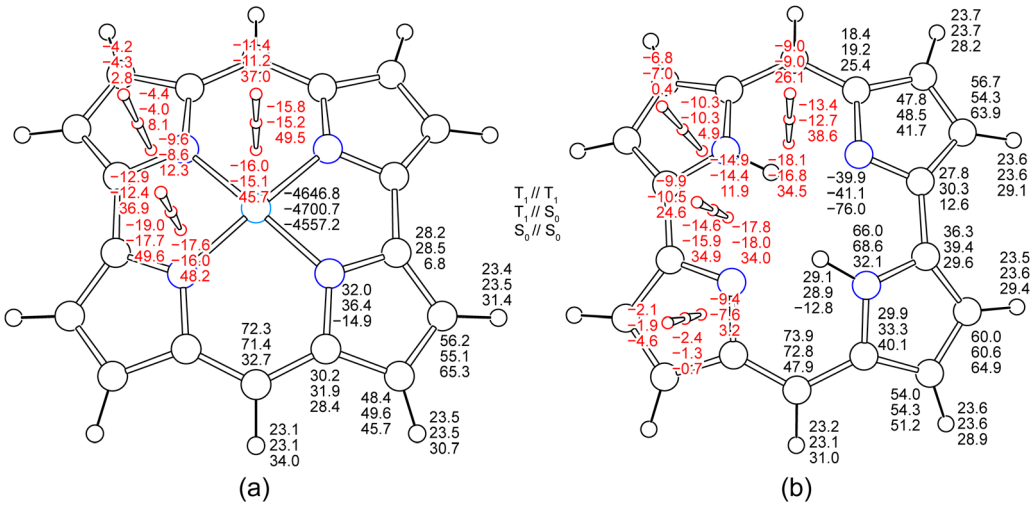

Fig. 3 Symmetry unique NICS values (in red) and carbon, nitrogen and hydrogen isotropic shieldings (in black) for the S_0 and T_1 electronic states of (a) NiNc and (b) H_2Nc, arranged in columns of three numbers each including, from bottom to top, $S_0//S_0$, $T_1//S_0$ and $T_1//T_1$ results (in ppm). $T_1//T_1$ data were obtained at the respective T_1 UB3LYP-D3(BJ) local minimum geometries. The NICS(+1) positions are above the bowl (closer to the viewer), and the NICS(−1) positions are inside the bowl. Other details as for Fig. 2.

the $T_1//T_1$ NICS values are slightly less negative than their $T_1//S_0$ counterparts which can be attributed to the choices of the positions at which the NICS(0) and NICS(±1) values are evaluated. The S_0 NICS(0) and NICS(1) values for the planar Ni^{II} porphyrin complex (NiP), calculated at a level of theory identical to that used in the current work, B3LYP-GIAO/6-311++G(d,p)/B3LYP-D3(BJ)/def2-TZVP, and at positions in and above the "internal cross" defined analogously to those for NiNc and H_2Nc, are −21.7 and −18.0 ppm, respectively,[22] which suggests that the "internal crosses" in the T_1 states of NiNc and H_2Nc are not that far off in their levels of aromaticity. Apart from the changes in the NICS values, the aromaticity reversals between the S_0 and T_1 states of NiNc and H_2Nc are also well-illustrated by the parallel changes in the hydrogen isotropic shieldings. The "external" hydrogens, connected to α and *meso* carbon atoms, are much more shielded in the S_0 states of the two molecules than they are in the respective T_1 states. On the other hand, the "internal" hydrogens in H_2Nc which are strongly deshielded in S_0, become strongly shielded in T_1.

The $\sigma_{iso}(\mathbf{r})$ isosurfaces for S_0 and T_1 electronic states of NiNc and H_2Nc are shown in Fig. 4. The $\sigma_{iso}(\mathbf{r})$ isosurfaces for the S_0 electronic states of the two molecules were drawn using Gaussian cube files taken from ref. 4. The isovalues of $\sigma_{iso}(\mathbf{r})$ = ±12 ppm were chosen so as to provide optimal levels of detail; isosurfaces for other isovalues for the T_1 states can be inspected using the Gaussian cube files provided in the ESI.†

The S_0 $\sigma_{iso}(\mathbf{r})$ isosurfaces illustrate the antiaromatic deshielded "internal crosses" and the aromatic shielded "halos" in NiNc and H_2Nc which were discussed in detail in ref. 4. As expected from the changes in the NICS values between the S_0 and T_1 states (Fig. 3), the sizeable deshielded regions enclosing the "internal crosses" in S_0 disappears in T_1, except for a small deshielded region surrounding the Ni atom. This is

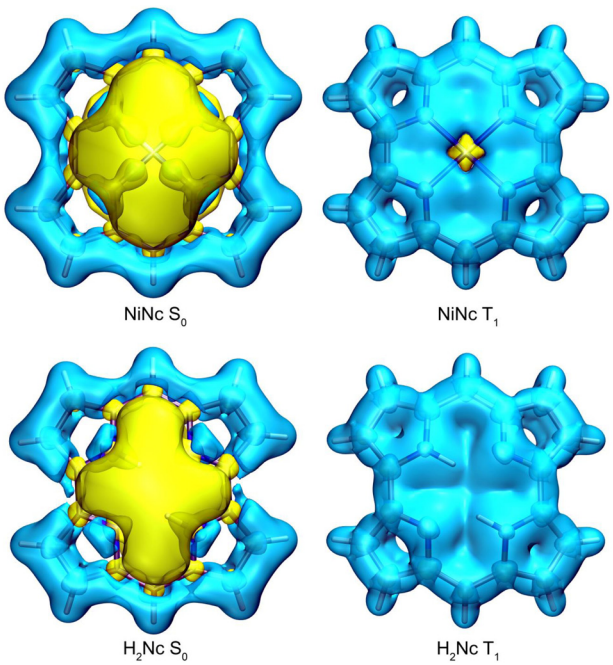

Fig. 4 Isotropic magnetic shielding around the S_0 and T_1 electronic states of NiNc and H_2Nc (looking at the top of each bowl). Isosurfaces at $\sigma_{iso}(\mathbf{r})$ = +12 ppm (shielded regions, blue) and $\sigma_{iso}(\mathbf{r})$ = −12 ppm (deshielded regions, yellow). $S_0//S_0$ and $T_1//T_1$ results as in Fig. 3.

a strong indication that the T_1 states of NiNc and H_2Nc become fully aromatic and do not retain any traces of antiaromatic behaviour. The T_1 $\sigma_{iso}(\mathbf{r})$ = 12 ppm isosurfaces for NiNc and H_2Nc feature depressions above the bowls across their "internal crosses", more pronounced in H_2Nc, which are not present in the S_0 $\sigma_{iso}(\mathbf{r})$ = 12 ppm isosurface for the planar NiP.[22] The NICS(+1) "internal cross" positions (above the bowls) fall

within these depressions (Fig. 3) which explains their lower values. The regions under the bowls are better shielded overall and there are no such depressions in the respective parts of the T_1 $\sigma_{iso}(\mathbf{r})$ = 12 ppm isosurfaces for NiNc and H_2Nc. The S_0 aromatic shielded ''halos'' shift towards the interiors of the molecules in T_1 and more closely follow the individual C–C, C_α–H and C_{meso}–H bonds; the T_1 shielding pictures over these bonds in both molecules closely resemble those in the S_0 state of NiP.[22] In fact, it is more accurate to say that in the T_1 states the aromatic shielded ''halos'' merge with the shielded ''internal crosses'' to produce Baird-aromatic triplet systems with 24 π electrons each.

As discussed previously,[4,22] the carbon and nitrogen atoms in the S_0 states of NiNc, H_2Nc and NiP are surrounded by small ovoid deshielded regions inside which $\sigma_{iso}(\mathbf{r})$ becomes negative; such regions can be also observed in the T_1 states of NiNc and H_2Nc. Small deshielded regions of this type often occur around sp^2 hybridized first main row atoms (see, for example, ref. 42). The presence of such deshielded regions around the carbon and nitrogen atoms in the S_0 and T_1 states of NiNc and H_2Nc suggests that the respective hybridization states of these atoms are close to sp^2, as in the S_0 state of NiP, despite the non-planar bowl-shaped geometries of the two states, and we can still talk of (mostly) π and σ electrons. The deshielded surroundings of the Ni atom which in the S_0 state of NiNc are submerged within the ''internal cross'' deshielded region are in line with the negative isotropic shieldings of this atom in the S_0 and T_1 states (Fig. 3) and with the positive NPA charges on these atoms (Fig. S1, ESI†).

The NPA charges for the S_0, T_1 and S_1 states of NiNc and H_2Nc (Fig. S1, ESI†) indicate that the respective electronic density distributions are significantly less sensitive to the change of the electronic state than are the nuclear isotropic shieldings (Fig. 3). For example, whereas the σ_{iso} values for the protons inside the ''internal cross'' in H_2Nc change sharply, from *ca.* −13 to 29 ppm between S_0 and T_1 (Fig. 3), the corresponding NPA charges increase by just 0.002*e* (Fig. S1, ESI†). Similarly to the bond lengths (Fig. 2) and shielding data (Fig. 3), the NPA charges (Fig. S1, ESI†) highlight the close similarity between the UB3LYP and TDA-B3LYP descriptions of the T_1 states of NiNc and H_2Nc, as well as the less close but still well-defined similarity between the UB3LYP/TDA-B3LYP descriptions of the T_1 states and the TDA-B3LYP descriptions of the S_1 states of the two molecules.

Conclusions

The comparison between the NICS values and isotropic shielding pictures for the S_0 and T_1 electronic states of Ni^{II} norcorrole and norcorrole strongly suggests that the antiaromatic features in the S_0 states of the two molecules, the two very similar strongly deshielded antiaromatic ''internal crosses'' including 16 atoms and 16 π electrons, undergo aromaticity reversals upon excitation. As a result of these aromaticity reversals both ''internal crosses'' become well-shielded all over and merge with the peripheral aromatic ''halos'' which do not change much between S_0 and T_1 to produce Baird-aromatic triplet systems with 24 π electrons each. This is supported by the changes in the HOMA values between the optimized geometries of the S_0 and T_1 states of NiNc and H_2Nc. The similarities between the optimized geometries of the T_1 and S_1 states of NiNc and H_2Nc and between the corresponding HOMA values strongly suggest that the two molecules experience analogous aromaticity reversals in their S_1 states.

Somewhat counterintuitively, the geometries of the fully aromatic T_1 and S_1 states of NiNc and H_2Nc turn out to have larger bowl depths and so are more non-planar than the corresponding S_0 geometries at which both molecules display widely recognized antiaromatic features. The increases in bowl depth are a consequence of the decreases of the C_α–C_α bond lengths, changes that at the same time make the T_1 and S_1 geometries more aromatic and less planar.

The very low $T_1 \leftarrow S_0$ and $S_1 \leftarrow S_0$ vertical and adiabatic excitation energies of NiNc and H_2Nc support the notion of antiaromatic destabilization of the S_0 states and aromatic stabilization of the T_1 and S_1 states of the two molecules and indicate that both of T_1 and S_1 in each molecule are easily accessible from S_0. These observations suggest that the photochemistry of NiNc and H_2Nc and their derivatives would be an interesting area for experimental and theoretical research. The changes in the bowl depts of NiNc and H_2Nc upon excitation could be exploited in the design of new low-amplitude ''flapping'' fluorophores, complementing the well-known group of higher-amplitude ''flapping'' fluorophores based on π-expanded cyclooctatetraenes and oxepins.[11–13]

Author contributions

P. B. K. suggested the study of excited state aromaticity reversals in norcorrole, carried out the DFT calculations, and wrote the original draft. E. C. calculated the HOMA values. Both authors discussed the results and contributed to the final manuscript.

Data availability

The data supporting this article have been included as part of the ESI.†

Conflicts of interest

There are no conflicts to declare.

Acknowledgements

The authors are grateful for the support of this work by the University of York.

Notes and references

1 M. Bröring, S. Köhler and C. Kleeberg, *Angew. Chem., Int. Ed.*, 2008, **47**, 5658–5660.
2 T. Ito, Y. Hayashi, S. Shimizu, J.-Y. Shin, N. Kobayashi and H. Shinokubo, *Angew. Chem., Int. Ed.*, 2012, **51**, 8542–8545.
3 A. Ghosh, I. H. Wasbotten, W. Davis and J. C. Swarts, *Eur. J. Inorg. Chem.*, 2005, 4479–4485.
4 P. B. Karadakov, *Org. Lett.*, 2020, **22**, 8676–8680.
5 R. Nozawa, H. Tanaka, W.-Y. Cha, Y. Hong, I. Hisaki, S. Shimizu, J.-Y. Shin, T. Kowalczyk, S. Irle, D. Kim and H. Shinokubo, *Nat. Commun.*, 2016, **7**, 13620.
6 T. Yonezawa, S. A. Shafie, S. Hiroto and H. Shinokubo, *Angew. Chem., Int. Ed.*, 2017, **56**, 11822–11825.
7 N. C. Baird, *J. Am. Chem. Soc.*, 1972, **94**, 4941–4948.
8 B. Durbeej, J. Wang and B. Oruganti, *ChemPlusChem*, 2018, **83**, 958–967.
9 B. Oruganti, J. Wang and B. Durbeej, *Org. Lett.*, 2017, **19**, 4818–4821.
10 J. Wang, B. Oruganti and B. Durbeej, *ChemPhotoChem*, 2019, **3**, 450–460.
11 T. Yamakado, S. Takahashi, K. Watanabe, Y. Matsumoto, A. Osuka and S. Saito, *Angew. Chem., Int. Ed.*, 2018, **57**, 5438–5443.
12 R. Kimura, H. Kuramochi, P. Liu, T. Yamakado, A. Osuka, T. Tahara and S. Saito, *Angew. Chem., Int. Ed.*, 2020, **59**, 16430–16435.
13 R. Kotani, L. Liu, P. Kumar, H. Kuramochi, T. Tahara, P. Liu, A. Osuka, P. B. Karadakov and S. Saito, *J. Am. Chem. Soc.*, 2020, **142**, 14985–14992.
14 B. J. Lampkin, Y. H. Nguyen, P. B. Karadakov and B. VanVeller, *Phys. Chem. Chem. Phys.*, 2019, **21**, 11608–11614.
15 L. J. Karas, C.-H. Wu, H. Ottosson and J. I. Wu, *Chem. Sci.*, 2020, **11**, 10071–10077.
16 M. Rosenberg, C. Dahlstrand, K. Kilså and H. Ottosson, *Chem. Rev.*, 2014, **114**, 5379–5425.
17 R. Papadakis and H. Ottosson, *Chem. Soc. Rev.*, 2015, **44**, 6472–6493.
18 J. Yan, T. Slanina, J. Bergman and H. Ottosson, *Chem. – Eur. J.*, 2023, **29**, e202203748.
19 M. Kataoka, *J. Chem. Res.*, 2004, 573–574.
20 P. B. Karadakov, *J. Phys. Chem. A*, 2008, **112**, 7303–7309.
21 P. B. Karadakov, *J. Phys. Chem. A*, 2008, **112**, 12707–12713.
22 P. B. Karadakov and T. Riley, *Chem. – Eur. J.*, 2023, **29**, e202203400.
23 J. Kruszewski and T. M. Krygowski, *Tetrahedron Lett.*, 1972, **13**, 3839–3842.
24 T. M. Krygowski, H. Szatylowicz, O. A. Stasyuk, J. Dominikowska and M. Palusiak, *Chem. Rev.*, 2014, **114**, 6383–6422.
25 J. C. Dobrowolski, *ACS Omega*, 2019, **4**, 18699–18710.
26 P. V. R. Schleyer, C. Maerker, A. Dransfeld, H. Jiao and N. J. R. V. E. Hommes, *J. Am. Chem. Soc.*, 1996, **118**, 6317–6318.
27 P. v R. Schleyer, H. Jiao, N. J. R. v E. Hommes, V. G. Malkin and O. Malkina, *J. Am. Chem. Soc.*, 1997, **119**, 12669–12670.
28 H. Fallah-Bagher-Shaidaei, C. S. Wannere, C. Corminboeuf, R. Puchta and P. V. R. Schleyer, *Org. Lett.*, 2006, **8**, 863–866.
29 M. J. Frisch, G. W. Trucks, H. B. Schlegel, G. E. Scuseria, M. A. Robb, J. R. Cheeseman, G. Scalmani, V. Barone, G. A. Petersson, H. Nakatsuji, X. Li, M. Caricato, A. V. Marenich, J. Bloino, B. G. Janesko, R. Gomperts, B. Mennucci, H. P. Hratchian, J. V. Ortiz, A. F. Izmaylov, J. L. Sonnenberg Williams, F. Ding, F. Lipparini, F. Egidi, J. Goings, B. Peng, A. Petrone, T. Henderson, D. Ranasinghe, V. G. Zakrzewski, J. Gao, N. Rega, G. Zheng, W. Liang, M. Hada, M. Ehara, K. Toyota, R. Fukuda, J. Hasegawa, M. Ishida, T. Nakajima, Y. Honda, O. Kitao, H. Nakai, T. Vreven, K. Throssell, J. A. MontgomeryJr, J. E. Peralta, F. Ogliaro, M. J. Bearpark, J. J. Heyd, E. N. Brothers, K. N. Kudin, V. N. Staroverov, T. A. Keith, R. Kobayashi, J. Normand, K. Raghavachari, A. P. Rendell, J. C. Burant, S. S. Iyengar, J. Tomasi, M. Cossi, J. M. Millam, M. Klene, C. Adamo, R. Cammi, J. W. Ochterski, R. L. Martin, K. Morokuma, O. Farkas, J. B. Foresman and D. J. Fox, *Gaussian 16 Revision A.03*, Gaussian, Inc., Wallingford CT, 2016.
30 M. J. G. Peach, M. J. Williamson and D. J. Tozer, *J. Chem. Theory Comput.*, 2011, **7**, 3578–3585.
31 A. Chantzis, A. D. Laurent, C. Adamo and D. Jacquemin, *J. Chem. Theory Comput.*, 2013, **9**, 4517–4525.
32 T. Lu and F. Chen, *J. Comput. Chem.*, 2012, **33**, 580–592.
33 E. M. Arpa and B. Durbeej, *Phys. Chem. Chem. Phys.*, 2023, **25**, 16763–16771.
34 E. Matito, J. Poater, M. Duran and M. Solà, *J. Mol. Struct. THEOCHEM*, 2005, **727**, 165–171.
35 J. C. Dobrowolski and P. F. J. Lipiński, *RSC Adv.*, 2016, **6**, 23900–23904.
36 V. Gogonea, P. V. R. Schleyer and P. R. Schreiner, *Angew. Chem., Int. Ed.*, 1998, **37**, 1945–1948.
37 P. W. Fowler, E. Steiner and L. W. Jenneskens, *Chem. Phys. Lett.*, 2003, **371**, 719–723.
38 Z. Rinkevicius, J. Vaara, L. Telyatnyk and O. Vahtras, *J. Chem. Phys.*, 2003, **118**, 2550–2561.
39 J. Vaara, *Phys. Chem. Chem. Phys.*, 2007, **9**, 5399–5418.
40 K. Aidas, C. Angeli, K. L. Bak, V. Bakken, R. Bast, L. Boman, O. Christiansen, R. Cimiraglia, S. Coriani, P. Dahle, E. K. Dalskov, U. Ekström, T. Enevoldsen, J. J. Eriksen, P. Ettenhuber, B. Fernández, L. Ferrighi, H. Fliegl, L. Frediani, K. Hald, A. Halkier, C. Hättig, H. Heiberg, T. Helgaker, A. C. Hennum, H. Hettema, R. Hjertenæs, S. Høst, I.-M. Høyvik, M. F. Iozzi, B. Jansík, H. J. A. Jensen, D. Jonsson, P. Jørgensen, J. Kauczor, S. Kirpekar, T. Kjærgaard, W. Klopper, S. Knecht, R. Kobayashi, H. Koch, J. Kongsted, A. Krapp, K. Kristensen, A. Ligabue, O. B. Lutnæs, J. I. Melo, K. V. Mikkelsen, R. H. Myhre, C. Neiss, C. B. Nielsen, P. Norman, J. Olsen, J. M. H. Olsen, A. Osted, M. J. Packer, F. Pawlowski, T. B. Pedersen, P. F. Provasi, S. Reine, Z. Rinkevicius, T. A. Ruden, K. Ruud, V. V. Rybkin, P. Sałek, C. C. M. Samson.,

A. Sánchez de Merás, T. Saue, S. P. A. Sauer, B. Schimmelpfennig, K. Sneskov, A. H. Steindal, K. O. Sylvester-Hvid, P. R. Taylor, A. M. Teale, E. I. Tellgren, D. P. Tew, A. J. Thorvaldsen, L. Thøgersen, O. Vahtras, M. A. Watson, D. J. D. Wilson, M. Ziolkowski and H. Ågren, *Wiley Interdiscip. Rev.: Comput. Mol. Sci.*, 2014, **4**, 269–284; Dalton, a molecular electronic structure program, Release Dalton2021.alpha, 2021, see **https://daltonprogram.org**.

41 P. B. Karadakov and S. Saito, *Angew. Chem., Int. Ed.*, 2020, **59**, 9228–9230.

42 P. B. Karadakov, P. Hearnshaw and K. E. Horner, *J. Org. Chem.*, 2016, **81**, 11346–11352.